In press on ApJ (Main Journal)

Effects of Tidal Interactions on the Gas Flows of Elliptical Galaxies

A. D'Ercole[1], S. Recchi[2,3]

and

L. Ciotti[1,4]

[1]Osservatorio Astronomico di Bologna, via Ranzani 1, 40127 Bologna, ITALY

[2]Dip. di Astronomia, Università di Bologna, via Ranzani 1, 40127 Bologna, ITALY

[3]SISSA/ISAS, via Beirut 2-4, 34014 Trieste, ITALY

[4]Scuola Normale Superiore, Piazza dei Cavalieri 7, 56126 Pisa, ITALY

ABSTRACT

During a Hubble time, cluster galaxies may undergo several mutual encounters close enough to gravitationally perturb their hot, X–ray emitting gas flows. We ran several 2D, time dependent hydrodynamical models to investigate the effects of such perturbations on the gas flow inside elliptical galaxies, focusing on the expected X–ray properties. In particular, we studied in detail the modifications occurring in the scenario proposed by D'Ercole et al. (1989), in which the galactic interstellar medium produced by the aging galactic stellar population, is heated by type Ia supernovae (SNIa) at a decreasing rate. We find that, although the tidal interaction in our models lasts less than 1 Gyr, its effect extends over several Gyrs. The tidally induced turbulent flows create dense filaments which cool quickly and accrete onto the galactic center, producing large spikes in the global X–ray luminosity $L_{\rm X}$. Once this mechanism starts, it is fed by gravity and amplified by SNIa. This evolution is found to be virtually independent of the dynamical state of the gas flow at the beginning of the interaction. To better understand the role of SNIa heating, we also considered a "pure" cooling flow model without supernovae; in this case the amplitude of the $L_{\rm X}$ fluctuations due to the tidal interaction is substantially reduced. We conclude that, if SNIa significantly contribute to the energetics of the gas flows in ellipticals, then the observed spread in the $L_{\rm X} - L_{\rm B}$ diagram at any fixed optical galaxy luminosity $L_{\rm B} \gtrsim 3 \times 10^{10} L_{\odot}$ may be caused, at least in part, by this mechanism. On the contrary, tidal interactions cannot be responsible for the observed spread if the pure cooling flow scenario applies.

Subject headings: Galaxies: cooling flows – Galaxies: elliptical and lenticular, cD – Galaxies: interactions – Galaxies: ISM – X-rays: galaxies

1. INTRODUCTION

In a previous paper D'Ercole et al. (1989) proposed the wind–outflow–inflow (WOI) scenario as a possible explanation for one of the most striking properties of the X–ray emission of elliptical galaxies, i.e., the large scatter in the $L_{\rm X} - L_{\rm B}$ diagram of roughly two orders of magnitude in $L_{\rm X}$ at any fixed $L_{\rm B} \gtrsim 3 \times 10^{10} L_{\odot}$ (Fabbiano 1989, Fabbiano, Kim & Trinchieri 1992). In their subsequent extensive exploration of 1D hydrodynamical models Ciotti et al. (1991, hereafter CDPR) assumed that the type I supernova (SNIa) rate decreases in time as $R_{\rm SN} \propto t^{-1.5}$, faster than the decrease of the mass return rate from the (passively) evolving stellar population, which varies in time approximately as $t^{-1.36}$. In these models, the gas lost by the stars is initially driven out of the galaxy through a supersonic wind powered by the thermalization of the kinetic energy injected in the interstellar medium (ISM) by the SNIas. As the specific energy input decreases, the wind turns into a subsonic outflow and eventually the flow reverts to an inflow regime, at the time of the so–called *cooling catastrophe* ($t_{\rm cc}$). In pace with the content of the X–ray emitting hot gas, $L_{\rm X}$ decreases during the wind phase and increases during the outflow regime up to a maximum reached at $t_{\rm cc}$. Later on, $L_{\rm X}$ slowly decreases roughly following the quenching of the SNIa heating $L_{\rm SN} \propto R_{\rm SN}$. CDPR ran several 1D numerical simulations, showing how $t_{\rm cc}$ critically depends on the values of the structural parameters of the host galaxy, such as the scale–length of the stellar distribution (e.g, the effective radius for de Vaucouleurs profiles or the so–called core radius for King profiles), the scale–length of the dark matter halo, the relative amount of total masses of the two distributions. Small changes in one (or more) of these parameters produce a large shift (of the order of some Gyr) of $t_{\rm cc}$, causing two galaxies of virtually the same $L_{\rm B}$ to be caught at very different $L_{\rm X}$ after a Hubble time. As a consequence, the above–mentioned $L_{\rm X}$ scatter at fixed $L_{\rm B}$ finds a simple explanation in the WOI scenario.

The main objection raised against this scenario has been the claimed detection of low iron abundance in the ISM of ellipticals. In fact, under the assumption of solar abundance ratios, the analysis of the available data suggests a very low iron abundance, consistent with no SNIas enrichment, and even lower than that of the stellar component (Ohashi et al. 1990, Awaki et al. 1991, Ikebe et al. 1992, Serlemitsos et al. 1993, Loewenstein et al. 1994, Awaki et al. 1994, Arimoto et al. 1997, Matsumoto et al. 1997). However, some authors have found that more complex multitemperature models with a higher abundance give a better fit to the data (Kim et al. 1996, Buote & Fabian 1998). This is rather puzzling, in that a value as high as one fourth of the standard Tammann (1982) rate $R_{\rm SN} = 0.22$ SNU (for $H_0 = 50$ km s^{-1} Mpc^{-1}) agrees with the current optical estimates of the present day SNIa rate (Cappellaro et al. 1997). Several models have been calculated with this new rate (Pellegrini & Ciotti 1998, D'Ercole & Ciotti 1998, hereafter DC), resulting in the main features of the WOI scenario being preserved, provided the amount of dark matter is properly scaled down.

In any case, even though $R_{\rm SN} \approx 0$, it is well known that the pure cooling flow scenario is unable, in isolated galaxies, to reproduce the observed scatter (see, e.g., CDPR). As a consequence, the possible environmental origin of the $L_{\rm X} - L_{\rm B}$ scatter has been proposed. Although some

discussion was dedicated to environmental effects, the bulk of the CDPR simulations did not consider ambient influences. It is known, however, that the majority of early type galaxies is found in clusters, where they certainly suffer several environmental interactions. More specifically, 1) thermal conduction with the intracluster medium (ICM); 2) ram pressure stripping of the ISM due to the motion of the galaxies with respect to the ICM; 3) influence of the cluster tidal field; 4) galaxy–galaxy gravitational encounters.

Because the ICM in rich clusters is much hotter ($T \simeq 10^8$ K) than the galactic gas flows ($T \simeq 10^7$ K), heat is expected to flow into the galactic ISM if thermal conduction is not suppressed by magnetic fields. It is easy to show that the heat transferred by an unimpeded thermal conduction is much larger than any other galactic energy budget, and evaporation can hardly be avoided. The very existence of bright X–ray ellipticals thus suggests that heat conduction must be suppressed to a great extent (see, e.g., CDPR, and references therein).

The ram pressure effect of the ICM on the ISM of the elliptical galaxies was discussed by D'Ercole et al. (1993) in the WOI scenario, and, e.g., by Balsara, Livio & O'Dea (1994, and references therein) in the cooling flow scenario. While numerical models show that ram pressure is very effective in stripping galaxies of gas, observations reveal that numerous cluster galaxies are strong X–ray emitters, thus showing their ability to retain their hot ISM. For example, Dow & White (1995), found that ellipticals in Coma are as X–ray bright as in Virgo. This situation appears rather puzzling, and certainly not satisfactorily understood.

The mean cluster gravitational field acts on the structure of each galaxy and its gaseous halo, as a weak tidal field. N–body numerical simulations (e.g., Ciotti & Dutta, 1994) show that its effect on the galactic stellar component is very small, consisting essentially in a re–orienting of the galactic major axis with respect to the cluster center.

In summary, while some effort was spent by several authors in considering the influence of the ICM on the ISM of ellipticals, up to now no attempt was made to study the response of the X–ray emitting ISM of cluster ellipticals to the tidal interaction due to the cluster field and to a close encounter with a nearby galaxy. As we will see, in a typical cluster, encounters close enough to have non negligible dynamical effects on the ISM are likely to occur.

In this paper we show the results of 2D numerical hydrodynamical models focusing on the influence both of the cluster tidal field and of a transient external gravitational field on the evolution of the ISM of ellipticals in the WOI and cooling flow scenarios. In §2 we describe the galaxy model, the hydrodynamical equations, and the assumptions adopted in our simulations. The results are presented in §3. A discussion and the conclusions are finally given in §4.

2. The Galaxy Model

In order to better compare the present results with those obtained by CDPR, we adopt for the model galaxy the same bright and dark matter (DM) distributions considered by these authors for their basic model (the so–called *King Reference Model*, KRM). The stellar density distribution is a truncated King (1972) model

$$\rho_*(r) = \frac{\rho_{*0}}{(1 + r^2/r_*^2)^{3/2}}, \quad r \le r_{\rm t}, \tag{1}$$

and the DM density profile is a truncated quasi–isothermal model

$$\rho_{\rm h}(r) = \frac{\rho_{\rm h0}}{1 + r^2/r_{\rm h}^2}, \quad r \le r_{\rm t}. \tag{2}$$

Here (ρ_{*0}, r_*) and $(\rho_{\rm h0}, r_{\rm h})$ are the central density and scale–length of the luminous and DM density distributions, respectively, while $r_{\rm t}$ is their common truncation radius. The total galaxy density, potential, and mass are $\rho_{\rm g} = \rho_* + \rho_{\rm h}$, $\phi_{\rm g} = \phi_* + \phi_{\rm h}$, and $M_{\rm g} = M_* + M_{\rm h}$.

As for the KRM in CDPR we assume $\rho_{*0} = 6.08 \times 10^{-21}$ g cm^{-3}, $\rho_{\rm h0} = 7.6 \times 10^{-23}$ g cm^{-3}, $r_* = 368$ pc, $r_{\rm h} = 4.5 r_*$ and $r_{\rm t} = 66.24$ kpc. With these parameters $M_* = 2.75 \times 10^{11} M_\odot$ and $M_{\rm h} = 2.48 \times 10^{12} M_\odot$, respectively, and the galaxy lies on the so–called Fundamental Plane. It should be noted that several recent indications, from high–resolution N–body simulations (Dubinski & Carlberg 1991; Navarro, Frenk & White 1997) as well as from theoretical arguments (Evans & Collett 1997; Ciotti 1996,1999), seem to suggest a peaked density distribution for the DM halos, as for example that used in the numerical simulations of gas flows carried out by Pellegrini & Ciotti (1998). In spite of this, we decided to maintain here the functional form for the halo as in the KRM, in order to better understand the effects of the tidal interactions by comparison with the unperturbed model.

Of course, a self–consistent treatment of the evolution of galactic gas flows in the cluster environment is a formidable task, both for the complexity of the involved physics, and for the high dimensionality of the parameter space (requiring very large computational resources to be fully explored). Our aims are far more narrow, focusing on the qualitative understanding of the effects of a representative tidal encounter. In this line, the mass $M_{\rm p}$ of the perturbing galaxy (the *perturber*) is assumed to be equal to the mass of the galaxy, $M_{\rm p} = M_{\rm g} \simeq 2.8 \times 10^{12} M_\odot$, because we are not interested here in the effects of interactions with significantly less massive galaxies. In a subsequent paper (Pellegrini, D'Ercole & Ciotti, in preparation) we explore the effects produced on the X–ray emission of a galaxy model similar to that here discussed by a collision with a significantly less massive cluster galaxy.

2.1. Assumptions and Equations

We derive and discuss here the hydrodynamical equations describing the evolution of the gas flows in our models, using the general equations given in Appendix A.2. In the following, bold–face

symbols represent vectors. In the (baricentric) cluster inertial reference frame S, the center of mass of the galaxy and of the perturber are $\mathbf{R}$ and $\mathbf{R}_{\rm p}$, respectively; moreover, $\mathbf{r}_{\rm p} = \mathbf{R}_{\rm p} - \mathbf{R}$ and $r_{\rm p} = ||\mathbf{r}_{\rm p}||$, where $||\cdot||$ is the standard norm. For computational reasons these equations are written in a non–inertial reference system S' fixed by the following rules: the origin of S' coincides with $\mathbf{R}$, $\boldsymbol{\xi}$ is the position vector in S', the ξ_3 axis points at all times towards $\mathbf{R}_{\rm p}$, and finally $r = ||\boldsymbol{\xi}||$.

2.1.1. The Effective Gravitational Field

We derive first the effective gravitational field experienced by the gas in the frame S' (see equation [A16]), and we discuss two assumptions used in our models, namely that 1) the cluster tidal field is negligible during the encounter, and that 2) the perturber trajectory can be approximated by a straight line, covered with constant velocity. Although in the numerical code the gravitational forces are not approximated by their linear expansion (tidal regime), here we consider the associated tidal fields, in order to obtain the geometrical conditions for the validity of the assumptions above.

At any position $\mathbf{x}$ in the cluster frame S, the total acceleration is $\mathbf{g} = -\nabla_{\mathbf{x}}(\phi_{\rm cl} + \phi_{\rm p} + \phi_{\rm g})$, where $\phi_{\rm cl}$, $\phi_{\rm p}$, and $\phi_{\rm g}$ are the cluster, perturber, and galaxy potentials, respectively, and $\nabla_{\mathbf{x}}$ is the gradient operator with respect to $\mathbf{x}$. Note that the self–gravity of the gaseous component is not considered. The acceleration $\mathbf{A}$ of the center of mass of the galaxy is given by $M_{\rm g}\mathbf{A} = -\int \rho_{\rm g}\nabla_{\mathbf{x}}(\phi_{\rm cl} + \phi_{\rm p})d^3\mathbf{x}$. In the tidal approximation $\phi_{\rm cl}$ and $\phi_{\rm p}$ are expanded up to the second order around $\mathbf{R}$, i.e.,

$$\phi_{\rm cl}(\mathbf{x}) \sim \phi_{\rm cl}(\mathbf{R}) - < \mathbf{g}_{\rm cl}(\mathbf{R}), \mathbf{x} - \mathbf{R} > - \frac{< T_{\rm cl}(\mathbf{R})(\mathbf{x} - \mathbf{R}), \mathbf{x} - \mathbf{R} >}{2}, \tag{3}$$

where $\mathbf{g}_{\rm cl}(\mathbf{R}) = -\nabla_{\mathbf{R}}\phi_{\rm cl}(\mathbf{R})$, $<,>$ is the standard inner product, and $T_{\rm cl}$ is the tidal tensor associated with $\phi_{\rm cl}$, whose elements are given by

$$T_{\rm cl,ij}(\mathbf{R}) = -\frac{\partial^2\phi_{\rm cl}(\mathbf{R})}{\partial R_i \partial R_j}, \quad (i, j = 1, 2, 3). \tag{4}$$

A similar relation holds for the gravitational field produced by the perturber, where now $\mathbf{g}_{\rm p}(\mathbf{R}) = -\nabla_{\mathbf{R}}\phi_{\rm p}(\mathbf{R})$ and $T_{\rm p}$ is the tidal tensor associated with $\phi_{\rm p}$. In this approximation, simple calculations show that the effective gravitational field entering equation (A16) is given by

$$\mathbf{g} - \mathbf{A} \sim [T_{\rm cl}(\mathbf{R}) + T_{\rm p}(\mathbf{R})](\mathbf{x} - \mathbf{R}) + \mathbf{g}_{\rm g}, \tag{5}$$

where $\mathbf{g}_{\rm g} = -\nabla_{\mathbf{x}}\phi_{\rm g}$. The coordinate transformation from S to S' shows that

$$\mathcal{O}^{\rm T}\mathbf{g}_{\rm g} = -G\frac{M_{\rm g}(r)}{r^3}\boldsymbol{\xi}, \tag{6}$$

and

$$\mathcal{O}^{\rm T}[T_{\rm p}(\mathbf{R})(\mathbf{x} - \mathbf{R})] = -\frac{GM_{\rm p}}{r_{\rm p}^3}(\xi_1, \xi_2, -2\xi_3). \tag{7}$$

Equations (6) and (7) are derived under the assumption of spherical mass distributions. Actually, the galaxy and the perturber will change their shape during the interaction. However, for small deformations the potential remains rounder than the underlying density distribution (see, e.g., Binney & Tremaine 1987, hereafter BT), and so we regard equation (6) as still largely valid for our problem. Moreover, the effect of the deformation of the pertuber density influences the tidal tensor $T_{\rm p}$ given in equation (7) only at higher order in $r_{\rm p}$ (see, e.g., Danby 1962, Chapter 5). As a consequence, in all simulations the (visible and dark) mass densities of the galaxy and of the pertuber are assumed to maintain their initial spherical symmetry.

As anticipated in point 1) above, in our simulations we do not consider the term $T_{\rm cl}$ appearing in equation (5), in order to reduce the dimensionality of the parameter space. The influence of the cluster tidal field in absence of close encounters was explored separately, and it is discussed in §4. We now determine when the perturber tidal field $T_{\rm p}$ is dominant over $T_{\rm cl}$. The cluster tidal field at distance $R = ||\mathbf{R}||$ from the cluster center is given by equation (4), and its explicit expression is

$$T_{\rm cl}(\mathbf{R}) = -\frac{4\pi G\overline{\rho_{\rm cl}}(R)}{3}\begin{pmatrix}1 & 0 & 0\\ 0 & 1 & 0\\ 0 & 0 & 3q-2\end{pmatrix}, \tag{8}$$

where $\overline{\rho_{\rm cl}}(R) = 3M_{\rm cl}(R)/4\pi R^3$ is the cluster mean density inside R, and $0 \leq q(R) = \rho_{\rm cl}(R)/\overline{\rho_{\rm cl}}(R) \leq 1$. The matrix expression of $T_{\rm cl}$ is obtained in the reference frame S with its z axis aligned along $\mathbf{R}$ (see, e.g., Ciotti & Dutta 1994). As a consequence, in equation (8) the *radial* and the *tangential* components of the cluster tidal field are apparent[1]. In order to obtain a simple estimate of the relative importance of the cluster and pertuber tidal fields, we consider a typical cluster with a density profile $\rho_{\rm cl}$ as that given in equation (1), with a core radius $r_{\rm cl} = 350$ kpc, and a central velocity dispersion $\sigma_{\rm cl} = 10^3$ km s^{-1} (Sarazin 1986). We compare the *minimum* (absolute) value of the perturber tidal field components, $GM_{\rm p}/r_{\rm p}^3$, with the radial and tangential components of the cluster tidal field. In Fig. 1 these quantities are showed, and it turns out that the cluster tidal field can be neglected for $r_{\rm p} \simeq 100$ kpc everywhere but inside the cluster core.

2.1.2. The Pertuber Trajectory

Following the arguments above, we assumed in our simulations $r_{\rm p}^{\rm min} = 100$ kpc as the minimum distance during the encounter, in order to safely neglect the cluster tidal force on the ISM. Actually, the (full) perturber gravitational field is taken into account for distances much larger than $r_{\rm p}^{\rm min}$, i.e., for $r_{\rm p} \leq 450$ kpc. This in order to avoid a sudden change in the total gravitational field experienced by the gas flow, that could be at the origin of unphysical oscillations. In other words, up to the time $t_{\rm p}^{\rm i}$ (a free parameter in the simulations, whose choice

---

[1]Note that the tidal field outside a spherical mass distribution given in equation (7) can be obtained directly from equation (8) for $q = 0$, and by substitution of $\rho_{\rm cl}$ with $\rho_{\rm p}$.

is given in §3) the gas flow evolves as in CDPR, successively the perturber is placed at a distance of 450 kpc, with an initial velocity of $V = 1000$ km s^{-1} relative to the galaxy. We indicate with $t_{\rm m}$ the time at which $r_{\rm p}(t_{\rm m}) = r_{\rm p}^{\rm min}$, and with $\Delta t_{\rm p} = t_{\rm m} - t_{\rm p}^{\rm i}$.

In order to follow the time evolution of the ISM, we obviously need to know how $r_{\rm p}$ changes with time. Adopting equation (3) to describe the effect of the cluster gravitational field on the galaxy and pertuber motions, one obtains

$$\ddot{\mathbf{r}}_{\rm p} \sim -G(M_{\rm g} + M_{\rm p})\frac{\mathbf{r}_{\rm p}}{r_{\rm p}^3} + T_{\rm cl}(\mathbf{R})\mathbf{r}_{\rm p}. \tag{9}$$

With the assumed parameters for the galaxy, the perturber, and the cluster density distribution, it is easy to verify from the equation above that the effects of $T_{\rm cl}$ on the motion of the two galaxies are non negligible for values of $r_{\rm p}$ in the range of interest, and so the relative orbit cannot be described by a two–body problem. As anticipated by point 2) in §2.1.1, we arbitrarily adopt a linear trajectory for $\mathbf{r}_{\rm p}$, described at constant velocity V. In this assumption $\Delta t_{\rm p} \simeq 460$ Myr, and simple geometrical arguments show that the only non–zero component of the angular velocity in S', entering equation (A16), is given by:

$$|\Omega_1| = \frac{r_{\rm p}^{\rm min} V}{V^2(t - t_{\rm m})^2 + (r_{\rm p}^{\rm min})^2}. \tag{10}$$

We point out that, as a consequence of the geometry of the problem, the non–inertial forces associated with the rotation of S' cannot be taken into consideration by our 2D code, and so we drop these terms in the hydrodynamical equations used in the numerical simulations (equations [12]-[14]). In §4 we will calculate *a posteriori*, from the computed models, the ratio between the gravity and the fictitious forces associated with $\boldsymbol{\Omega}$, in order to obtain a rough estimate of the severity of this approximation. Although this assumption may appear rather rough, the computed models show that the perturbations in the ISM do not depend on the details of the physical process which generate them. Thus our assumption is not particularly severe.

2.1.3. The Source Terms

As already discussed in the literature (Mathews & Baker 1971), the mass and energy sources in elliptical galaxies are associated with their evolving stellar population: the two main contributions are due to the gas lost by the red giants and to the ejecta of SNIas. The total mass return rate, expressed in the general case in equations (A15)-(A17), is given here by $\mathcal{M} = \alpha(t)\rho_*$, where $\alpha(t) = \alpha_*(t) + \alpha_{\rm SN}(t)$. We adopt the same $\alpha(t)$ as in CDPR (equations [3] and [7] there). In particular, this corresponds to a present day $R_{\rm SN} = 0.15$ SNU, i.e., 2/3 of the standard Tammann's rate. Moreover, we assume that the internal energy associated with the mass ejection in both processes is negligible with respect to the thermalization of the stellar velocity dispersion and to the SNIa ejection velocity. The *exact* expression for the *injection energy* is given by

$$\mathcal{E}_0 = \frac{\alpha_* u_*^2 + \alpha_{\rm SN} u_{\rm SN}^2}{2\alpha} + \frac{{\rm Tr}(\sigma^2)}{2} \simeq \frac{\alpha_{\rm SN} u_{\rm SN}^2 + \alpha_* {\rm Tr}(\sigma^2)}{2\alpha}, \tag{11}$$

where the last formula is derived under the hypothesis that 1) the velocity of stellar winds is considerably lower than the stellar velocity dispersion (i.e., $u_*^2 << \sigma^2$), and that 2) the stellar velocity dispersion is lower than the velocity of SNIa ejecta (i.e., $\sigma^2 << u_{\rm SN}^2$). In accordance with the previous works we adopt the second, approximate expression for $\mathcal{E}_0$, but we remind that in some circumstances the full one should be used. The cooling rate per unit volume is given by $\mathcal{L} = n_{\rm e} n_{\rm p} \Lambda(T)$, where we parametrize $\Lambda(T)$ following the prescription of Mathews & Bregman (1978), after correction of a wrong sign in their equation (A2). Finally, no streaming velocity of the stellar component is assumed to be present in S', and accordingly in the momentum and energy equations (A16)-(A17) we set $\overline{\mathbf{v}}' = 0$. This assumption can be qualitatively explained considering that, when the mutual interaction between the galaxy and the perturber starts, their stellar and dark matter distributions are distorted. These deformations are responsible for the appearance of a net torque acting on the galaxy density distribution, from which an angular momentum is originated. Of course, the real situation is much more complex, but our simple assumptions should capture the kinematical behavior of the galaxy stellar and dark matter components.

2.1.4. The Hydrodynamical Equations

As a consequence of all the previous assumptions and discussions, equations (A15)-(A17) are specialized in the numerical code as follows:

$$\frac{\partial \rho}{\partial t} + \nabla_{\boldsymbol{\xi}} \cdot \rho \boldsymbol{\nu} = \alpha \rho_*, \tag{12}$$

$$\frac{\partial \rho \boldsymbol{\nu}}{\partial t} + \nabla_{\boldsymbol{\xi}} \cdot (\rho \boldsymbol{\nu} \otimes \boldsymbol{\nu}) = \rho (\mathbf{g}_{\rm g} + T_{\rm p} \boldsymbol{\xi}) - (\gamma - 1) \nabla_{\boldsymbol{\xi}} E, \tag{13}$$

$$\frac{\partial E}{\partial t} + \nabla_{\boldsymbol{\xi}} \cdot E \boldsymbol{\nu} = -(\gamma - 1) E \nabla_{\boldsymbol{\xi}} \cdot \boldsymbol{\nu} + \frac{\alpha \rho_*}{2} ||\boldsymbol{\nu}||^2 + \alpha \rho_* \mathcal{E}_0 - \mathcal{L}. \tag{14}$$

ρ, E, and $\boldsymbol{\nu}$ are respectively the density, the internal energy per unit volume, and the velocity of the gas, expressed in S'. The explicit expressions of $\mathbf{g}_{\rm g}$ and $T_{\rm p}\boldsymbol{\xi}$ in this frame are given in equations (6) and (7). The gas pressure is $p = (\gamma - 1)E$, where $\gamma = 5/3$ is the ratio of the specific heats. To integrate the set of equations we used a second–order, upwind, 2D numerical code described in DC, coupled with a staggered, spherical, Eulerian grid. Given the symmetry of the problem, the grid covers polar angles $0^\circ \leq \theta \leq 180^\circ$ with 82 equally spaced angular zones. The radial coordinate is divided into 72 zones and extends up to 95 kpc. In order to get a reasonable spatial resolution in the inner region, a geometrical progression is adopted for the radial mesh size, the first one being 100 pc wide. Reflecting boundary are assumed everywhere but at the outer boundary, where outflow conditions are adopted. With the adopted non–inertial reference frame S' and numerical grid, the perturber is always outside the grid and moves along the $\theta = 0$ direction (i.e., along the ξ_3 axis). As in CDPR, the gas temperature is not allowed to drop below 10^4 K, to avoid an excessive reduction of the time step when a rapid cooling is present. We assume

the model galaxy to be initially devoid of gas due to the previous activity of the Type II SNe. A discussion on the reliability and implications of this assumption is given in CDPR.

3. The Models

Given the Courant condition on the angular mesh close to the center, the time steps for the numerical computations are rather short (few 10^3 yr). We thus computed only few models. We first ran a model without the perturber and cluster gravitational field (hereafter model M0), i.e., a model analogous to the KRM presented in CDPR. As for the KRM, the cooling catastrophe occurs before 15 Gyr, and all the three dynamical phases – wind, outflow and inflow – are recovered[2].

In order to understand whether there are differences in the flow evolution depending on the time $t_{\rm m}$ at which the maximum approach happens, we ran three models (M1, M2, M3) for three different values of $t_{\rm m}$, namely $t_{\rm m}^{1,2,3} = (6.3, 10.8, 12.6)$ Gyr. In each of these models the initial conditions are given by the hydrodynamical quantities of model M0 at $t_{\rm p}^{\rm i} = t_{\rm m} - \Delta t_{\rm p}$. In model M1 the galaxy starts to be perturbed when it is still in its wind phase, while in models M2 and M3 the galaxy is perturbed when is in the outflow and inflow phase, respectively (see Fig. 3). We also ran a pure cooling flow model (hereafter model MC) in which the energy injection by SNIa is absent. For this model we set $t_{\rm p}^{\rm i} = 4.9$ Gyr. Although this model is expected to be rather similar to model M3, we ran it to ascertain whether the presence of the SNe energy input may affect the perturbed gas flow, even in the inflow phase.

Finally, we ran two more models without perturber, in order to check the sensitivity of our results to some of the assumptions made. Namely, 1) model MP is analogous to model M3, but with a *random* large–scale velocity field perturbation added to the initial conditions, as done by Kritsuk, Böhringer & Müller (1998) in their simulations; and 2) model MT is analogous to model MC, but with the cluster tidal field taken into account during a galaxy orbit inside the cluster.

3.1. Models Discussion

We discuss here in detail the M1 model, in which the galaxy starts to be perturbed during the wind phase. The other M2 and M3 models are presented by comparison with the M1 model, pointing out differences and analogies.

[2]Note however that in model M0 $t_{\rm cc}$ is greater than in the KRM (11 Gyr instead of 9.3 Gyr, see Fig. 3). This depends on the different value assumed for the mean molecular weight (0.62 instead of 0.5) which enters quadratically in the cooling term. By the way, this shows once more the extreme dependence of the WOI models on the parameter values.

3.1.1. Hydrodynamics

Figure 2 shows the density contours and the velocity field of the gas at four different times. Panel a is a shot taken at a time very close to $t_{\rm m}$, when the distance to the perturber is slightly larger than $r_{\rm p}^{\rm min}$; the exact time and relative distance are $(t, r_{\rm p})$=(6.4 Gyr, 141.4 kpc). The ISM in the galactic region facing the perturber accelerates toward the right direction (where the perturber is located), and is lost by the galaxy at higher velocity than in the opposite direction. This apparent asymmetry is due to the fact that in the code the full gravitational field of the perturber is considered, which, for short distances, differs significantly from the associated (symmetric) tidal field. In panel b ($t = 9.9$ Gyr) the effects of the encounter are still clearly visible, although the perturber distance from the galaxy (for the assumed rectilinear trajectory) is $r_{\rm p} = 3.6$ Mpc. This is also true at later times (panels c and d), where eddies are established and different dynamical regimes are present, some regions being in outflow and others in inflow, a situation analogous of that found in DC on their investigation on gas flows in (isolated) S0 galaxies.

3.1.2. X–ray Luminosity and Gas Mass Evolution

The X–ray luminosity evolution of model M1 is shown as a solid line in Fig. 3a. For comparison, the dashed line represents the $L_{\rm X}$ temporal evolution of the model M0, and the dotted line shows the time evolution of the SNIa energy input for unit time, $L_{\rm SN}$.

As the encounter with the perturber occurs, the cooling catastrophe is anticipated, as a consequence of the increase in the mean density in the galactic central regions produced by the tidal perturbation, and $L_{\rm X}$ reaches its (first) maximum at $t_{\rm cc} \simeq 9.4$ Gyr, earlier than for model M0 ($t_{\rm cc} \simeq 11$ Gyr). This is an interesting result. In fact, note that considering spherical coordinates with the ξ_3 polar axis ($\theta = 0°$) oriented towards the perturber (the coordinate system actually adopted in the numerical code), from equation (7) one obtains that the radial component of the tidal force (for unit mass) is given by $F_{\rm rad} = -(GM_{\rm p}r/r_{\rm p}^3)(\sin^2\theta - 2\cos^2\theta)$ and is *expansive* for $0° < \theta < \arctan\sqrt{2} \simeq 54°$ and $126° \lesssim \theta < 180°$. On the complementary spherical sector the field is *compressive*. Due to the strong non–linear dependence of the cooling function on the gas density, it is not easy to determine without the aid of numerical simulations which effect prevails in determining the successive evolution of the flow, i.e., if the cooling catastrophe is anticipated or retarded by the effect of the tidal field. Our results show that actually compression wins the game and cooling increases.

Successively, strong and fast oscillations in $L_{\rm X}$ occur, whose amplitude may reach an order of magnitude. These oscillations are due to correspondent oscillations of the ISM density in the galactic central regions: in fact, most of the X–ray luminosity is emitted there[3], for $L_{\rm X} \propto n^2$. It is

[3]Being $L_{\rm X} = \int n^2\Lambda(T)dV$, the oscillations in $L_{\rm X}$ are basically due to variations and/or rearrangements in the hot gas density, because $\Lambda(T)$ is nearly constant in the range of X–ray temperatures.

important to note that, while these density oscillations reflect dramatically on $L_{\rm X}$, they have little effect on the overall content of the hot gas which decreases monotonically in this phase, as shown in Fig. 3d (medium solid line).

This strongly unsteady evolution is due to the non–spherical gas accretion onto the galaxy central region. Converging to the center, non–radial gas streams interact and compress each other, giving rise to tongues of dense cold gas (see Fig. 4, where enlargements of the gas distribution and of the velocity field in the central region are shown). These tongues are rapidly accreted onto the galaxy center. When the compressed gas quickly cools, $L_{\rm X}$ suddenly increases. The cooled gas disappears in the center, leaving behind regions of low gas density which do not radiate efficiently and tend to expand as they are heated by SNIa: as a consequence $L_{\rm X}$ abruptly decreases. New streams of hot gas coming from the outer regions contrast the expansion of the gas close to the center and form new cold filaments. This cycle is fed by gravity and amplified by $L_{\rm SN}$. Actually, the hot gas mass decreases after every spike of $L_{\rm X}$ (Fig. 3d, medium solid line), while the cold gas mass increases specularly (Fig. 3d, light solid line). When the mass of the hot ISM is sufficiently reduced, $L_{\rm X}$ falls by nearly two orders of magnitude. Successively, the low density, non radiating hot gas is able to revert the flow on large scale, and a new wind phase starts (see Fig.3a and Fig.3d for $t \gtrsim 12$ Gyr).

The importance of SNIa in maintaining this cycle is apparent when considering the X–ray luminosity evolution of model MC, shown in Fig. 5. In this model, where $L_{\rm SN} = 0$, the oscillations of $L_{\rm X}$ have smaller amplitudes and the dramatic drop shown by the model M1 is absent. In fact, the $L_{\rm X}$ oscillations in model MC never exceed a factor of three relatively to the unperturbed cooling flow solution. Concerning the total mass budget (Fig.3d, heavy solid line), it is apparent its substantial reduction when compared to model M0 (Fig.3d, heavy dashed line). Thus, the tidal encounter is able to strip a significant fraction of ISM from the M1 model.

Figure 3bc show that models M2 and M3 (where the maximum approach happens in the outflow and inflow phase, respectively) exhibit $L_{\rm X}$ oscillations similar to model M1. It is however apparent that in these latter models the dramatic drop in $L_{\rm X}$ (occurring in model M1 at $t \simeq 12$ Gyr), is absent over an Hubble time. This is due to the fact that $L_{\rm SN}$ at the time of the encounter is lower than in model M1 (Fig.3abc, dotted line). Thus less energy is available to sustain a turbulent flow, and the $L_{\rm X}$ (and mass budget) evolution of models M2 and M3 is more similar to model MC.

The hot and cold ISM masses of models M2 and M3 (medium and light solid lines in Fig. 3ef) evolve in the same qualitative way as in model M1 (Fig. 3d). On the contrary, their total mass (heavy solid line) increases, at odd with model M1. This result at first could seem surprising because model M1 is in a wind phase for $t \gtrsim 12$ Gyr, and one could expect an easier degassing than in models M2 and M3. Actually, the hot gas density in model M1 is *lower* than in models M2 and M3 (as can be seen considering the amount of hot gas mass in the three models): as a consequence, the mass loss at the outskirts ($r = r_{\rm t}$) of the galaxies *increases* from model M1 to

model M3. In model M1 the mass loss rate is lower than the mass return rate from the evolving stellar population, $\alpha(t)M_*$, the opposite is true for models M2, and this explains the different time behavior of the total mass in the three models.

3.1.3. Surface Brightness

The surface brightness profiles of all computed models do not result strongly influenced by the tidal interaction. As a representative case we describe the X–ray surface brightness distribution $\Sigma_{\rm X}$ of model M1 only. During all the model evolution, the isophotes remain rather circular, although locally distorted, even for a viewing angle $\theta = 90°$ (i.e. a direction perpendicular to the line joining the galaxy and the perturber, where the effect is maximum). This can be seen in Fig. 6, where two sets of isophotes are superimposed, referring to $t = 9.9$ Gyr (solid lines) and $t = 11.1$ Gyr (dotted lines). These times correspond to a local maximum and minimum of $L_{\rm X}$, respectively (black dots in Fig. 3a). Radial cross sections of $\Sigma_{\rm X}$ are shown (after an angular mean) in Fig. 7. Note that when $L_{\rm X}$ is higher ($t = 9.9$ Gyr) the extra–luminosity is radiated mostly from the center, and so density oscillations here are by far more important than in the rest of the galaxy.

4. Discussions and Conclusions

In this paper we have investigated the consequences of a gravitational encounter on the dynamics of the hot, X–ray emitting ISM of cluster elliptical galaxies. We adopted a spherical model galaxy identical to the King Reference Model described in CDPR in order to better compare our results with the "standard" WOI picture. It turns out that once the gas is perturbed by the gravity of a galaxy passing nearby, it remains turbulent for the rest of the time. In fact, when the spherical symmetry is broken by the tidal interaction, non–radial streams converging toward the center merge thus compressing the gas, which quickly cools and "disappears" into the center. Some regions close to the center are then formed where the gas is rarefied and tends to expand as heated by the sourcess terms. This expansion is contrasted by the outer ISM which is falling to smaller radii, and new cold filaments are formed. From an observational point of view the most striking consequences are the large oscillations of $L_{\rm X}$ coupled to the oscillations of the gas density. These oscillations may have amplitudes ranging over two orders of magnitude while the X–ray surface brightness does not stray dramatically from spherical symmetry. Thus, at least for WOI models, the X–ray luminosity does not represent a good diagnostic of the dynamical state of the gas when tidal interactions are present.

The mechanism described above has been proven to be self–sustaining and independent of the external cause which initially originated it. In fact, we ran the model MP where, as anticipated in §3, the perturber is absent, the galaxy is at rest in a inertial reference system, and a random large–scale "noise" is superimposed on the initial velocity field. In model MP the maximum

allowed relative amplitude of the perturbation with respect to the unperturbed velocity field is 20 per cent. Apart from this, the initial conditions are the same as for model M3. The mass budget and $L_{\rm X}$ evolution of model MP are shown in Fig. 8, which should be compared with Fig. 3cf. As can be seen, this model behaves mostly as model M3. The spikes in $L_{\rm X}$ are somewhat larger, but this is due to our (arbitrary) choice of the maximum amplitude of the velocity perturbations. We point out that model MP is rather similar to models discussed by Kritsuk et al. (1998). However, a significant comparison between these models and model MP cannot be made because the latter authors stop their simulations after only 50 Myr, a time interval too short to predict the behaviour of the flow on cosmological times. The major insight derived from model MP is that *the evolution of perturbed WOI models is weakly dependent on the specific nature of the perturbation.*

We also ran a pure cooling flow model with a tidal perturbation (model MC): in this case the $L_{\rm X}$ oscillations are significantly reduced (approximately of a factor of ten) with respect to those exhibited by model M3. The most important consequence is that *tidal interactions cannot be at the origin of the spread in the* $L_{\rm X} - L_{\rm B}$ *diagram if the pure cooling flow scenario applies.*

As discussed in §2, in our simulations we neglected the cluster tidal field, which is present in equation (5). Although the magnitude of the cluster tidal field during the encounter is negligible (see §2.1.1), one can ask whether the *cumulative* effects of such field over cosmological times are significative. In order to check this possibility, as anticipated in §3 we ran the model MT, in which $L_{\rm SN} = 0$, no perturber is present, and only the cluster tidal field is considered. The resulting evolution of this model (not shown here) is very similar to that of model MC, but the amplitudes in the $L_{\rm X}$ oscillations are much reduced. We thus conclude that the cluster tidal field can be safely neglected when studying the effects of galaxy–galaxy encounters like those considered here on the X–ray properties of early–type galaxies.

Moreover, it must be added that the role of the cluster tidal field is further reduced by the fact that during a Hubble time a galaxy may experience several encounters of the type discussed here. A simple estimate of this number can be obtained as follows. Suppose that the galaxy belongs to a typical rich cluster like that described in §2.1.1, and containing $N_{\rm T} = 300$ galaxies, whose luminosity function is given by

$$\phi(L)dL = N_\star \left(\frac{L}{L_\star}\right)^{-\alpha} \exp\left(-L/L_\star\right) d\left(\frac{L}{L_\star}\right), \tag{15}$$

where $L_\star \simeq 4.74 \times 10^{10}\ L_\odot$, $\alpha = 5/4$ (Schechter 1976, Sarazin 1986), and with lower and upper limits of $10^8 L_\odot$ and ∞, respectively. Using simple geometrical arguments it is easy to show that, for an impact parameter less than or equal to $r_{\rm p}^{\rm min}$, the *mean* number of interactions per galaxy during an Hubble time $t_{\rm H}$ is given by

$$n_{\rm i} \simeq \frac{\sigma_{\rm cl} t_{\rm H}}{r_{\rm cl}} \left(\frac{r_{\rm p}^{\rm min}}{r_{\rm cl}}\right)^2 \frac{\kappa N_{\rm T}}{10}. \tag{16}$$

In the equation above κ is the fraction of the total number of galaxies with luminosity greater than $L_{\rm B}$. For example, $\kappa \simeq 0.01$ for $L_{\rm B} = 5 \times 10^{10} L_\odot$ (the luminosity of our galaxy model); $\kappa \simeq 0.1$ for

$L_{\rm B} = 1.6 \times 10^{10} L_{\odot}$ (one third of the luminosity of our galaxy model). It turns out that $n_{\rm i} \simeq 2$ for $\kappa = 0.01$. The same result is obtained considering galaxies with $L_{\rm B} \geq 1.6 \times 10^{10} L_{\odot}$ in a poor cluster (or loose groups), with $N_{\rm T} = 30$, $r_{\rm cl} = 200$ kpc and $\sigma_{\rm cl} = 250$ km s^{-1} (see, e.g., Bahcall 1998).

Obviously the above analysis does not apply to small compact galaxy groups containing only a few members. In fact, these systems are highly collisional, and the mean separation between galaxies is comparable to their dimensions (see, e.g., Kelm, Focardi, & Palumbo 1998). As a consequence, strong gravitational interactions are frequent, the evolution of gas flows is higly perturbed, and the results of our simulations can not be directly applied in this case.

From a more observational point of view, the importance of the discussion above is also strengthen by the fact that, while it is true that the majority of elliptical galaxies are found in clusters, the galaxies from which the $L_{\rm X} - L_{\rm B}$ diagrams are constructed are either in groups or in the Virgo cluster (which is less rich than the cluster assumed in our simulations). Hovewer, from the discussion above it results that the "turbulent" mechanism here described should be quite common in ellipticals in clusters and groups, while galaxies in compact groups can hardly avoid strong gravitational interactions, that should produce either strong variations in their X–ray luminosity or even substantial degassing.

As pointed out in §2.2, with the computed models available, we are now in the position to evaluate the error induced by neglecting the non–inertial forces associated with the rotation of the adopted reference frame. From an analysis of the model's velocity field at different times, it turns out that, when the perturber is closest, the Coriolis and centrifugal forces are larger than the gravitational forces only within a small volume (with a characteristic size of ~ 2 kpc) at the edge of the galaxy facing the perturber, where the total gravity is very low. Later ($t - t_{\rm m} \gtrsim 200$ Myr), the gravity largely prevails (by a factor 100–1000) all over the computational grid. This is mainly due to the fact that for the assumed orbit $||\boldsymbol{\Omega}|| \propto (t - t_{\rm m})^{-2}$ (see equation [10]), and so it quickly reduces after the encounter; moreover, the non inertial force associated with $\dot{\boldsymbol{\Omega}}$ vanishes when $r_{\rm p} = r_{\rm p}^{\rm min}$, and, for $|t - t_{\rm m}| > r_{\rm p}^{\rm min}/V \simeq 100$ Myr, $||\dot{\boldsymbol{\Omega}}|| \propto |t - t_{\rm m}|^{-3}$. As a consequence, we believe that our results are reliable, and, although neglecting the fictitious forces due to rotation may prevent from obtaining the exact values of the $L_{\rm X}$ spikes, the essential physics is captured by the computed models.

In conclusion, the main results of this work can be summarized as follows:

- In WOI models the $L_{\rm X}$ oscillations induced by tidal encounters last for several Gyrs after the encounter is over. The qualitative evolution of these oscillations is not strongly dependent on the flow phase (wind, outflow, or inflow) occurring when the encounter starts; moreover, they appear to be rather independent of the physical process generating them. The characteristic period of such oscillations is of the order of the sound crossing time of the hot gas in the galactic inner region. If the encounter happens quite early, when $L_{\rm SN}$ is still relatively high, then a catastrophic drop of $L_{\rm X}$ is produced. These oscillations can contribute to the

observed spread in the $L_\mathrm{X} - L_\mathrm{B}$ diagram for galaxies in clusters and groups. Of course, this mechanism cannot be at the origin of the L_X scatter in isolated galaxies.

- When compared to WOI models, the amplitude of the L_X oscillations in cooling flow models (with $L_\mathrm{SN} = 0$) is substantially reduced. As a consequence, tidal interactions cannot be at the origin of the observed spread in the $L_\mathrm{X} - L_\mathrm{B}$ diagram in the "pure" (no SNIa heating) cooling flow scenario.
- In all computed models, the X–ray surface brightness Σ_X does not appear to be strongly distorted by tidal interactions. However, the (angular mean) radial profile of Σ_X is steeper in the inner region in coincidence with the L_X spikes.
- We found that the tidal stripping due to the perturber is effective. In fact, approximately half of the gas content of the galaxy is lost in perturbed WOI models when compared to the unperturbed one. In our pure cooling flow model the fraction of lost mass is reduced to one fourth.
- The cluster tidal field *alone* appears to be ineffective in producing large L_X oscillations when compared to tidal interactions. Moreover, during a Hubble time, galaxies in clusters suffers several encounters of the kind described here, and so the importance of the cluster tidal field on the X–ray properties of early–type galaxies is further reduced.

We would like to thank Neta Bahcall, Giuseppe Bertin, James Binney, and Silvia Pellegrini for very useful discussions, and Giovanna Stirpe and Steven Shore for a careful reading of the manuscript. We also acknowledge the anonymous referee for very constructive comments. This work was partially supported by Italian MURST, contract CoFin98, and by ASI contracts, ASI-95-RS-152 and ASI-ARS-96-70.

A. The Hydrodynamical Equations with General Source Terms in Non–Inertial Reference Systems

In Appendix A.1 we present the treatment of mass, momentum, and energy source terms in hydrodynamics, in the general anisotropic case. In Appendix A.2 the hydrodynamical equations with general source terms are expressed in a non inertial reference frame.

A.1. The Source Terms

In the following treatment we assume the presence in the (inertial) reference system S of a single source field, the generalization to the case of more than one field being straightforward. $\mathbf{x} = x_i \mathbf{e}_i$ and $\mathbf{v} = v_i \mathbf{e}_i$ are the position and the velocity vectors in S, respectively. Let the

source field be described by a distribution function $f = f(\mathbf{x}, \mathbf{v}; t)$ (see, e.g., BT), so that $n(\mathbf{x}; t) = \int_{\Re^3} f\, d^3\mathbf{v}$ represents the number density of sources.

The *mass return* associated with the source field is given by the function $m = m(\mathbf{x}, \mathbf{v}, \mathbf{n}; t)$, where $\mathbf{n} = n_i \mathbf{e}_i$ is a unitary vector accounting for the possibility of *anisotropic* mass sources; the physical units of m are mass for unit time for unit solid angle. The total mass return per unit time, volume and solid angle associated with the source field is then given by $\mu(\mathbf{x}, \mathbf{n}; t) = \int_{\Re^3} m\, f\, d^3\mathbf{v}$. Finally, integrating over the whole solid angle, we obtain the total mass return rate per unit time and volume at $\mathbf{x}$:

$$\mathcal{M}(\mathbf{x}; t) = \int_{4\pi} \mu\, d^2\mathbf{n}. \tag{A1}$$

For example, for mass sources independent of the source velocity $\mathbf{v}$, $\mu(\mathbf{x}, \mathbf{n}; t) = nm$; moreover for an isotropic source field, $\mathcal{M}(\mathbf{x}; t) = 4\pi nm$.

The *momentum return* associated with the source field is given by the vectorial function $\mathbf{p} = m(\mathbf{x}, \mathbf{v}, \mathbf{n}; t)[\mathbf{v} + u_{\rm s}(\mathbf{x}, \mathbf{v}, \mathbf{n}; t)\mathbf{n}]$, where $u_{\rm s}$ is the modulus of the velocity of the material associated with the source field along $\mathbf{n}$ *with respect to the source velocity* $\mathbf{v}$. The total momentum per unit time, volume and solid angle associated with the source field is then given by $\boldsymbol{\pi}(\mathbf{x}, \mathbf{n}; t) = \int_{\Re^3} \mathbf{p}\, f\, d^3\mathbf{v}$. Finally, integrating over the whole solid angle,

$$\mathbf{P}(\mathbf{x}; t) = \int_{4\pi} \boldsymbol{\pi}\, d^2\mathbf{n}. \tag{A2}$$

In particular, for mass sources and ejection velocity independent of the source velocity $\mathbf{v}$, $\boldsymbol{\pi}(\mathbf{x}, \mathbf{n}; t) = nm[\overline{\mathbf{v}} + u_{\rm s}\mathbf{n}]$, where

$$n(\mathbf{x}; t)\overline{\mathbf{v}}(\mathbf{x}; t) = \int_{\Re^3} \mathbf{v}\, f\, d^3\mathbf{v} \tag{A3}$$

is the *source streaming velocity field*, $\overline{\mathbf{v}} = \overline{v}_i \mathbf{e}_i$ (see, e.g., BT). Moreover, if m and $u_{\rm s}$ are also isotropic, $\mathbf{P}(\mathbf{x}; t) = \mathcal{M}\overline{\mathbf{v}}$.

The *energy source* associated with the source field is made of the contributions of two distinct parts, i.e., the *internal energy source* and the *kinetic energy source*. The internal energy source is described (in analogy with the mass source) by the function $e = e(\mathbf{x}, \mathbf{v}, \mathbf{n}; t)$. The physical units of e are energy per unit time per unit solid angle per unit mass. The total internal energy per unit time, volume and solid angle associated with the source field is then given by $\epsilon(\mathbf{x}, \mathbf{n}; t) = \int_{\Re^3} m\, e\, f\, d^3\mathbf{v}$. Finally, integrating over the whole solid angle,

$$\mathcal{E}(\mathbf{x}; t) = \int_{4\pi} \epsilon\, d^2\mathbf{n}. \tag{A4}$$

In particular, for mass and internal energy sources independent of the velocity source $\mathbf{v}$, $\epsilon(\mathbf{x}, \mathbf{n}; t) = \mu e$. Moreover, in case of isotropy, $\mathcal{E}(\mathbf{x}; t) = \mathcal{M}e$. The kinetic energy source is given by $k = \frac{1}{2}m(\mathbf{x}, \mathbf{v}, \mathbf{n}; t)||\mathbf{v} + u_{\rm s}(\mathbf{x}, \mathbf{v}, \mathbf{n}; t)\mathbf{n}||^2$. The total kinetic energy per unit time, volume and solid

angle associated with the source field is then given by $\kappa(\mathbf{x},\mathbf{n};t) = \int_{\Re^3} k\, f\, d^3\mathbf{v}$. Finally, integrating over the whole solid angle,

$$\mathcal{K}(\mathbf{x};t) = \int_{4\pi} \kappa\, d^2\mathbf{n}. \tag{A5}$$

In particular, for mass sources and ejection velocity independent of the velocity source $\mathbf{v}$, $\kappa(\mathbf{x},\mathbf{n};t) = nm[||\overline{\mathbf{v}}||^2 + \mathrm{Tr}(\sigma^2) + u_\mathrm{s}^2 + 2u_\mathrm{s} < \mathbf{n}, \overline{\mathbf{v}} >]/2$, where $\mathrm{Tr}(\sigma^2)$ is the trace of the velocity dispersion tensor associated with the source motion:

$$n(\mathbf{x};t)\sigma_{ij}^2(\mathbf{x};t) = \int_{\Re^3} (v_i - \overline{v}_i)\,(v_j - \overline{v}_j)\, f\, d^3\mathbf{v}. \tag{A6}$$

Moreover, if m and u_s are also isotropic, $\mathcal{K}(\mathbf{x};t) = \mathcal{M}[||\overline{\mathbf{v}}||^2 + u_\mathrm{s}^2 + \mathrm{Tr}(\sigma^2)]/2$. *Note that a source field is called isotropic only if the functions m, $\mathbf{p}$, u_s and e are all independent of $\mathbf{n}$.*

A.2. The Hydrodynamical Equations in a Non–Inertial Reference System

The basic hydrodynamical equations with general source terms are here derived (in the inviscid case) by using the standard approach based on the *Reynolds Transport Theorem*. In fact, this formulation is particularly useful when moving to a non–inertial reference frame (see, e.g., Narasimhan 1993).

As usual, we denote with $D/Dt = \partial/\partial t + v_i \partial/\partial x_i$ the Lagrangian derivative when expressed in Eulerian form. After some manipulation of the conservation laws expressed in integral form, and application of the Transport Theorem, one obtains the *continuity* equation

$$\frac{D\rho}{Dt} + \rho\nabla_\mathbf{x} \cdot \mathbf{u} = \mathcal{M}. \tag{A7}$$

The three components of the *momentum* equation are given by

$$\rho\frac{D\mathbf{u}}{Dt} = \rho\mathbf{g} - \nabla_\mathbf{x} p + \mathbf{P} - \mathcal{M}\mathbf{u}, \tag{A8}$$

where $\mathbf{g}$ is the total physical acceleration and $p = p(\mathbf{x};t)$ is the *thermodynamical pressure*. Finally, the *energy* equation is derived:

$$\frac{DE}{Dt} + (E+p)\nabla_\mathbf{x} \cdot \mathbf{u} = \mathcal{E} + \mathcal{K} + \frac{\mathcal{M}}{2}||\mathbf{u}||^2 - < \mathbf{P}, \mathbf{u} > - \mathcal{L}. \tag{A9}$$

where E is the *internal energy* per unit volume, and $\mathcal{L}$ describes the radiative losses per unit volume and unit time. Note that thermal conduction is not considered here.

In case of a completely isotropic source field (the case of our model galaxies), the momentum and energy equations can be rewritten as:

$$\rho\frac{D\mathbf{u}}{Dt} = \rho\mathbf{g} - \nabla_\mathbf{x} p + \mathcal{M}(\overline{\mathbf{v}} - \mathbf{u}). \tag{A10}$$

and

$$\frac{DE}{Dt} + (E+p)\nabla_{\mathbf{x}} \cdot \mathbf{u} = \frac{\mathcal{M}}{2}||\mathbf{u} - \overline{\mathbf{v}}||^2 + \mathcal{M}\left[e + \frac{u_{\mathrm{s}}^2}{2} + \frac{\mathrm{Tr}(\sigma^2)}{2}\right] - \mathcal{L}. \tag{A11}$$

We move now from S to a non–inertial frame S'. As well known, the position, velocity, and acceleration vectors $\mathbf{x}$, $\dot{\mathbf{x}}$, $\ddot{\mathbf{x}}$ (in S) are related to the corresponding vectors in S' by

$$\mathbf{x} = \mathbf{R} + \mathcal{O}\boldsymbol{\xi}, \tag{A12}$$

$$\dot{\mathbf{x}} = \mathbf{V} + \mathcal{O}(\dot{\boldsymbol{\xi}} + \boldsymbol{\Omega} \wedge \boldsymbol{\xi}), \tag{A13}$$

$$\ddot{\mathbf{x}} = \mathbf{A} + \mathcal{O}[\ddot{\boldsymbol{\xi}} + 2\boldsymbol{\Omega} \wedge \dot{\boldsymbol{\xi}} + \dot{\boldsymbol{\Omega}} \wedge \boldsymbol{\xi} + \boldsymbol{\Omega} \wedge (\boldsymbol{\Omega} \wedge \boldsymbol{\xi})], \tag{A14}$$

where $\mathbf{R}(t)$, $\mathbf{V}(t)$ and $\mathbf{A}(t)$ are the position, velocity, and acceleration of the origin of S' (see, e.g., Arnol'd 1980). $\mathcal{O}(t) \in SO(3)$ is a rotation matrix, and $\boldsymbol{\Omega}$ is the dual of the antisymmetric matrix $\mathcal{O}^{\mathrm{T}}\dot{\mathcal{O}}$. Geometrically, $\boldsymbol{\Omega}$ is the angular velocity of S' with respect to S resolved along the basis of S'. When resolved in S, we have $\boldsymbol{\omega} = \mathcal{O}\boldsymbol{\Omega}$.

Now, the scalar continuity and energy equations are transformed in the corresponding equations in S'. First, the relation between the velocity field $\mathbf{u}(\mathbf{x};t)$ (in S) and $\boldsymbol{\nu}(\boldsymbol{\xi};t)$ (in S') is obtained from the definition of velocity field as Lagrangian derivative of the position vector, and so from equation (A13) $\mathbf{u}(\mathbf{x};t) = \mathbf{V} + \mathcal{O}[\boldsymbol{\nu}(\boldsymbol{\xi};t) + \boldsymbol{\Omega} \wedge \boldsymbol{\xi}]$. Second, in S', the expression for the Lagrangian derivative is $D/Dt = \partial/\partial t + \nu_i \partial/\partial \xi_i$, moreover, it is easily proved that $\nabla_{\mathbf{x}} \cdot \mathbf{u} = \nabla_{\boldsymbol{\xi}} \cdot \boldsymbol{\nu}$.

The transformation of continuity and energy equations is now immediate; some care is required for the momentum equation, when considering the Lagrangian derivative of the velocity. The final equations (for isotropic sources) in conservative form are

$$\frac{\partial \rho}{\partial t} + \nabla_{\boldsymbol{\xi}} \cdot \rho\boldsymbol{\nu} = \mathcal{M}, \tag{A15}$$

$$\frac{\partial \rho\boldsymbol{\nu}}{\partial t} + \nabla_{\boldsymbol{\xi}} \cdot (\rho\boldsymbol{\nu} \otimes \boldsymbol{\nu}) = \rho\mathcal{O}^{\mathrm{T}}(\mathbf{g} - \mathbf{A}) - \rho[2\boldsymbol{\Omega} \wedge \boldsymbol{\nu} + \dot{\boldsymbol{\Omega}} \wedge \boldsymbol{\xi} + \boldsymbol{\Omega} \wedge (\boldsymbol{\Omega} \wedge \boldsymbol{\xi})] - \nabla_{\boldsymbol{\xi}} p + \mathcal{M}\overline{\mathbf{v}}', \tag{A16}$$

$$\frac{\partial E}{\partial t} + \nabla_{\boldsymbol{\xi}} \cdot E\boldsymbol{\nu} = -p\nabla_{\boldsymbol{\xi}} \cdot \boldsymbol{\nu} + \frac{\mathcal{M}}{2}||\boldsymbol{\nu} - \overline{\mathbf{v}}'||^2 + \mathcal{M}\left[e + \frac{u_{\mathrm{s}}^2}{2} + \frac{\mathrm{Tr}(\sigma^2)}{2}\right] - \mathcal{L}. \tag{A17}$$

REFERENCES

Arimoto, N., Matsushita, K., Ishimaru, Y., Ohashi, T., & Renzini, A. 1997, ApJ, 477, 128

Arnol'd, V. 1980, Mathematical methods of classical mechanics, Springer-Verlag, New York

Awaki, H., Koyama, K., Kunieda, H., Takano, S., Tawara, Y., & Ohashi, T. 1991, ApJ, 366, 88

Awaki, H., et al. 1994, PASJ, 46, L65

Bahcall, N.A. 1998, in Formation of Structure in the Universe, Jerusalem Winter School, Cambridge University Press, 135

Balsara, D.S., Livio, M., & O'Dea, C.P. 1994, ApJ, 437, 83

Binney, J.J., & Tremaine, S. 1987, Galactic Dynamics, Princeton University Press, (BT)

Buote, D.A., & Fabian, A.C. 1998, MNRAS, 296, 977

Cappellaro, E., Turatto, M., Tsvetkov, D.Y., Bartunov, O.S., Pollas, C., Evans, R., & Hamuy, M. 1997, A&A, 322, 431

Ciotti, L. 1996, ApJ, 471, 68

Ciotti, L. 1999, ApJ, 520, 574

Ciotti, L., & Dutta, S.N. 1994, MNRAS, 276, 961

Ciotti, L., D'Ercole, A., Pellegrini, S., & Renzini, A. 1991, ApJ, 376, 380 (CDPR)

D'Ercole, A., Renzini, A., Ciotti, L., & Pellegrini, S. 1989, ApJ, 341, L9

D'Ercole, A., Ciotti, L., Pellegrini, S. & Renzini, A. 1993, in Dynamical and Chemical Evolution of Galaxies, eds. I.J. Danziger et al. (Garching: ESO), 615

D'Ercole, A., & Ciotti, L. 1998, ApJ, 494, 535 (DC)

Danby, J.M.A. 1962, Fundamentals of celestial mechanics, The Macmillan Company, New York

Dow, K.L., & White, S.D.M. 1995, ApJ, 439, 113

Dubinski, J., & Carlberg, R.G. 1991, ApJ, 378, 496

Evans, N.W., & Collett, J.L. 1997, ApJ, 480, L103

Fabbiano, G. 1989, ARA&A, 27, 87

Fabbiano, G., Kim, D.W., & Trinchieri, G. 1992, ApJS, 80, 531

Ikebe, Y., et al. 1992, ApJ, 384, L5

Kelm, B., Focardi, P., & Palumbo, G.G.C. 1998, A&A, 335, 912

Kim, D.W., Fabbiano, G., Matsumoto, H., Koyama, K., & Trinchieri, G. 1996, ApJ, 468, 175

King, I.R. 1972, ApJ, 174, L123

Kritsuk, A., Böhringer, H. & Müller, E. 1998, MNRAS, 301, 343

Loewenstein, M., et al. 1994, ApJ, 436, L75

Mathews, W.G. & Baker, J.C., 1971, ApJ, 170, 241

Mathews, W.G. & Bregman, J.N., 1978, ApJ, 224, 308

Matsumoto, H., Koyama, K., Awaki, H., Tsuru, T., Loewenstein, M., & Matsushita, K. 1997, ApJ, 482, 133

Navarro, J.F., Frenk, C.S., & White, S.D.M. 1997, ApJ, 490, 493

Narasimhan, M.N.L. 1993, Principles of Continuum Mechanics, John Wiley & Sons, New York

Ohashi, T., et al. 1990, in Windows on Galaxies, eds. G. Fabbiano, J.A. Gallagher, & A. Renzini (Dordrecht: Kluwer), 243

Pellegrini, S., & Ciotti, L. 1998, A&A, 333, 433

Sarazin, C.L. 1986 Rev.Mod.Phys., 58, 1

Schechter, P. 1976, ApJ, 203, 297

Serlemitsos, P.J., Loewenstein, M., Mushotzky, R., Marshall, F., & Petre, R. 1993, ApJ, 413, 518

Tammann, G. 1982, in Supernovae: A Survey of Current Research, ed. M. Rees & R. Stoneham (Dordrecht: Reidel), 371

Fig. 1.— The modulus of the dimensionless radial (solid line) and tangential (dashed line) component of the cluster tidal field, as a function of the cluster radius. The normalization constant is $|T_{\rm p}|^{\rm min} = GM_{\rm p}/r_{\rm p}^3$, for $r_{\rm p} = 100$ kpc. The explicit expression of the q function entering equation (8) can be found in Ciotti & Dutta (1994). The cluster mass is obtained by using the standard relation $4\pi G\rho_{\rm cl}(0)r_{\rm cl}^2 = 9\sigma_{\rm cl}^2$.

Fig. 2.— Logarithmic density distribution and velocity field of the gas in model M1 at different times. The perturber is on the right.

Fig. 3.— The upper panels show the evolution of $L_{\rm X}$ for the models M1, M2, and M3 (solid lines), for the model M0 (dashed lines), and $L_{\rm SN}$ (dotted lines). The two dots refer to the times indicated in Fig. 2bc, and Figs. 6 and 7. The evolution of the total gas mass (heavy lines), hot gas mass (medium lines), and cold gas mass (light lines) are shown in the lower panels. Dashed lines refer to model M0, solid lines to models M1, M2, and M3.

Fig. 4.— Logarithmic density distribution and velocity field of the gas in model M1 near the galactic center at two different times (in particular the left panel is the enlargment of the central region of Fig. 2b). The turbulent regime of the flow, and the transient cold filaments are apparent.

Fig. 5.— Time evolution of $L_{\rm X}$ for the cooling flow, tidally perturbed MC model (solid line). $L_{\rm X}$ of the same model without any perturbation (dashed line) is shown for comparison.

Fig. 6.— X–ray surface brightness $\Sigma_{\rm X}$ of model M1 at $t = 9.9$ Gyr (solid curves) and $t = 11.1$ Gyr (dotted curves). These times are the same as in panels b and c of Fig. 2. The perturber is located on the right. Labels are in kpc.

Fig. 7.— Radial distribution of the angular averaged surface brightness $\Sigma_{\rm X}$ shown in Fig. 6. Solid and dotted lines correspond to a $L_{\rm X}$ maximum and minimum, respectively (see the black dots in Fig.3a). $r_e = \sqrt{r_{\rm t} r_{\rm cl}} \simeq 4.9$ kpc is the effective radius of the stellar density distribution. $\Sigma_{\rm X}^{\rm max}$ is the central value of the X–ray surface brightness of model M0.

Fig. 8.— X–ray luminosity $L_{\rm X}$ and gas mass evolution for the model MP. In the upper panel the dotted line represents $L_{\rm SN}$. In the lower panel the evolution of the total gas mass (heavy line), hot gas mass (medium line), and cold gas mass (light line) is shown.

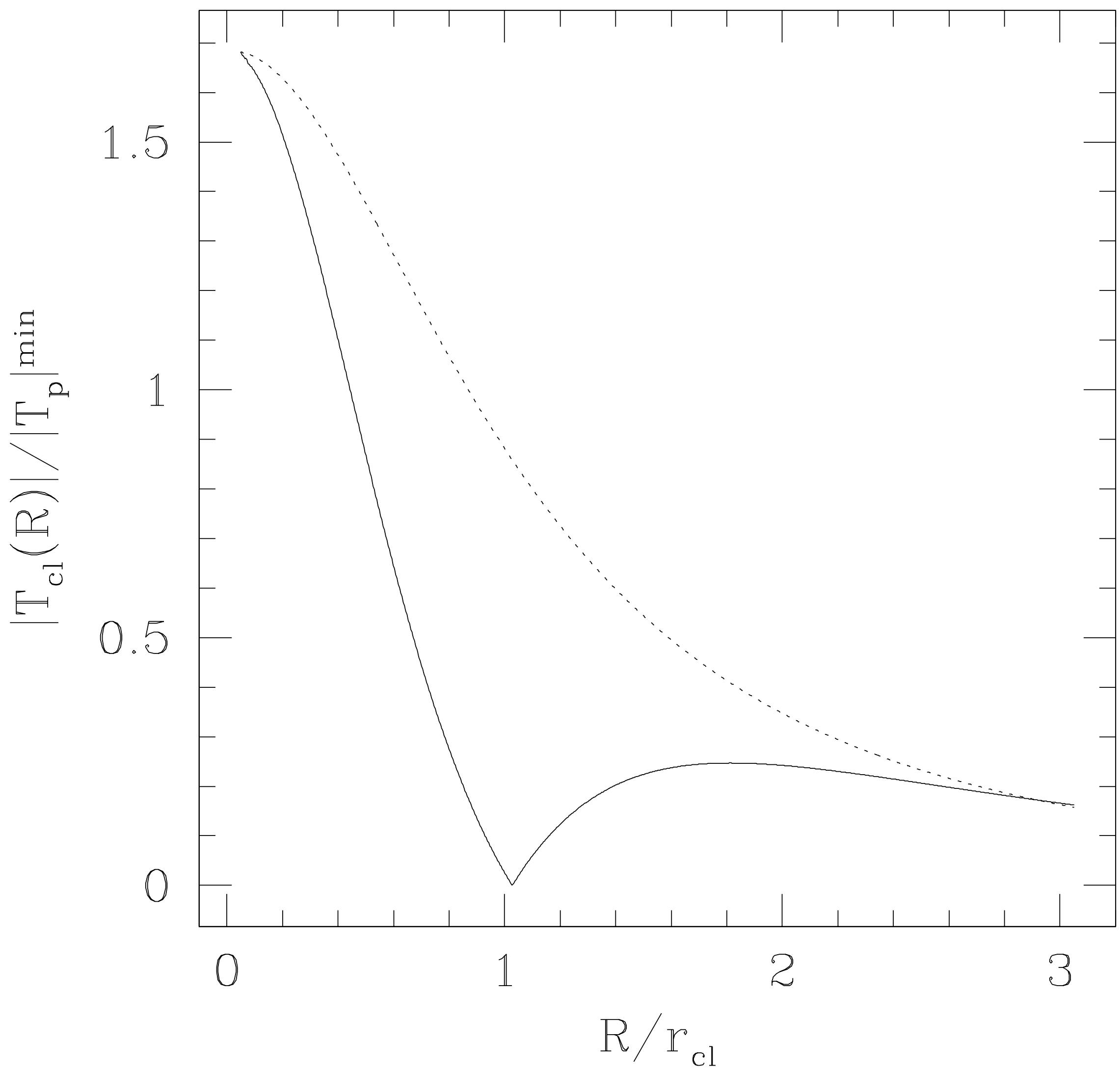

1.5
1
0.5
0
0
1
2
3
$|T_{cl}(R)|/|T_p|^{min}$
R/r_{cl}

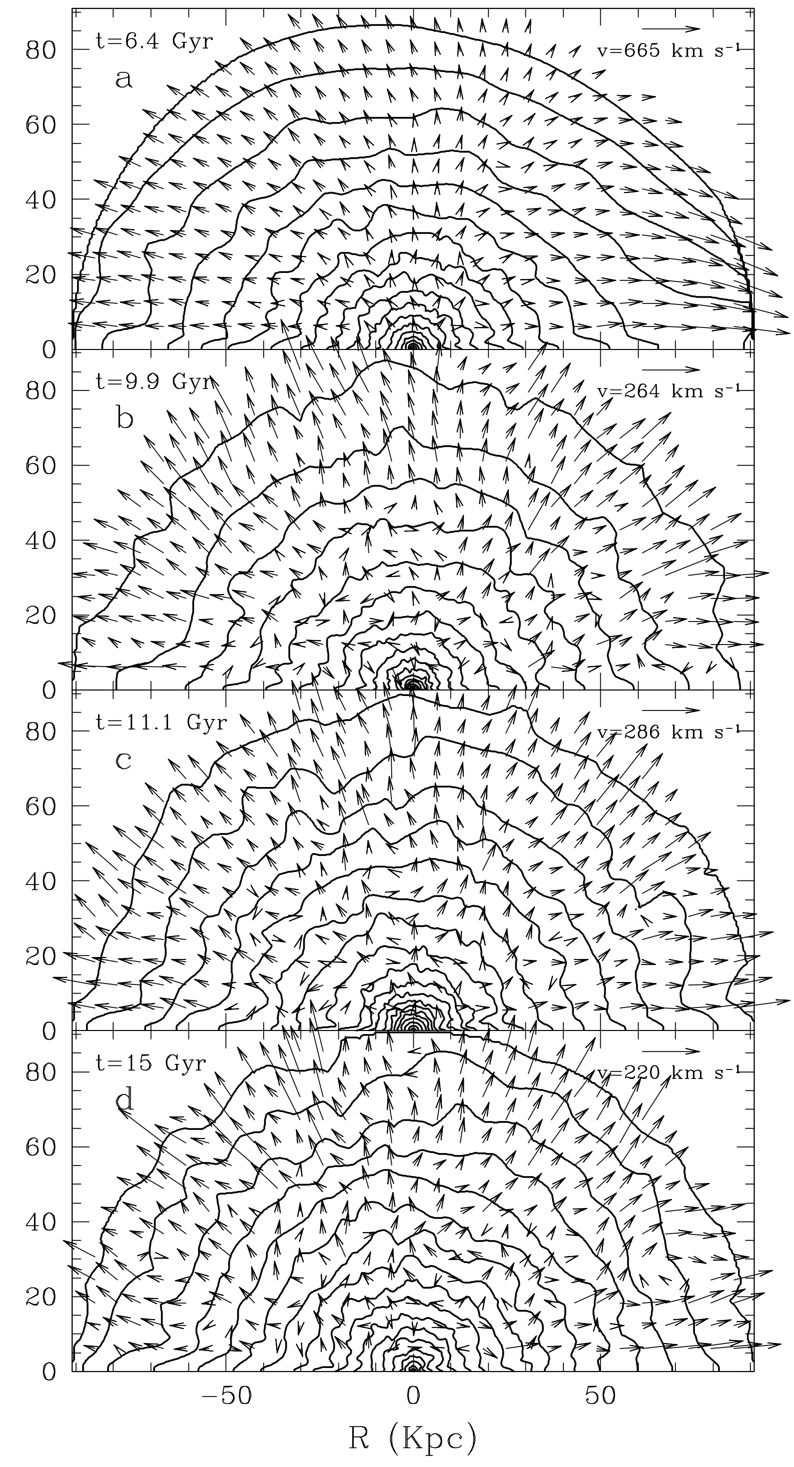

t=6.4 Gyr
v=665 km s⁻¹
a
t=9.9 Gyr
v=264 km s⁻¹
b
t=11.1 Gyr
v=286 km s⁻¹
c
t=15 Gyr
v=220 km s⁻¹
d
0
20
40
60
80
−50
0
50
R (Kpc)

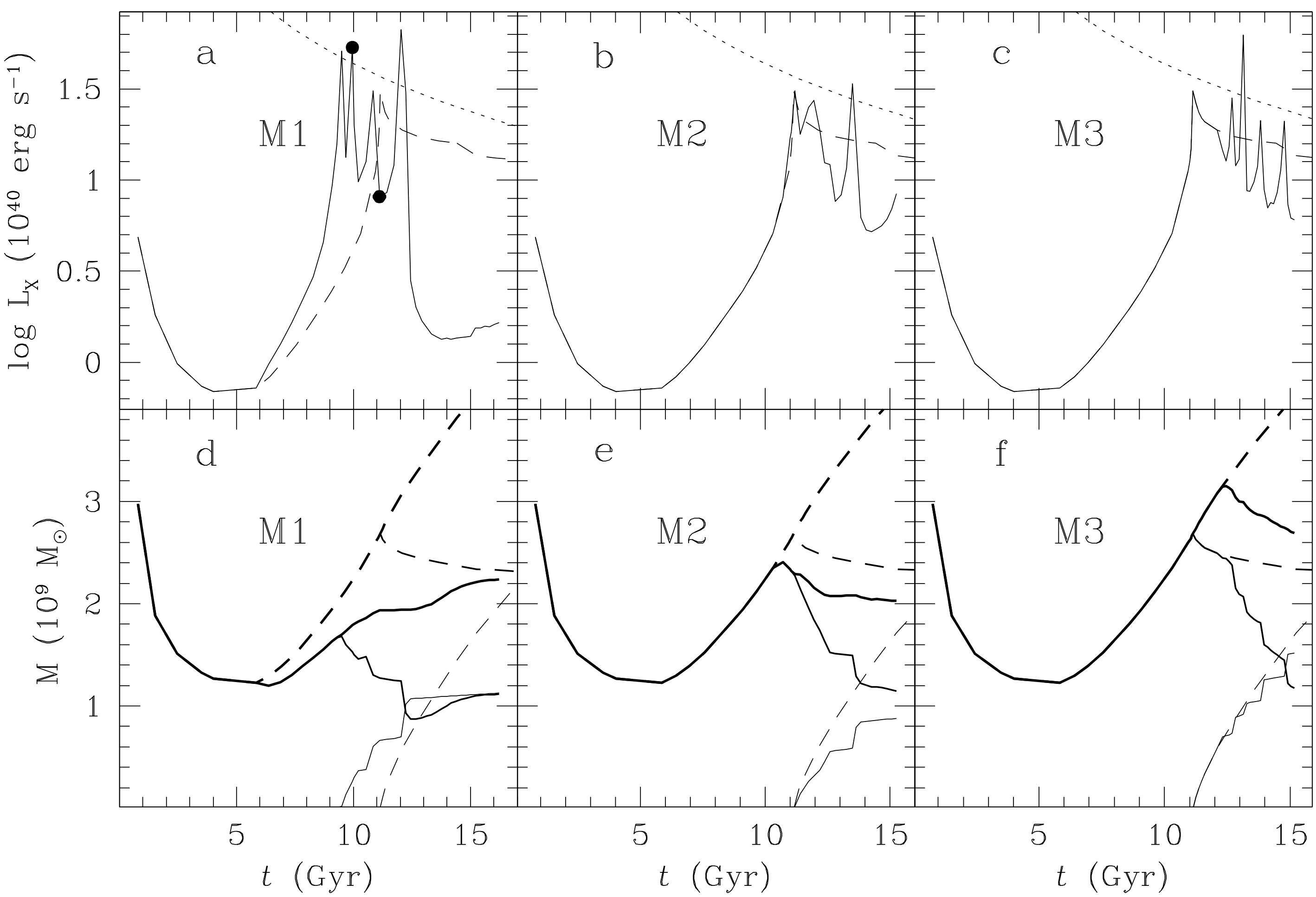

a
b
c
M1
M2
M3
d
e
f
log L_X (10^{40} erg s^{-1})
M (10^9 $M_\odot$)
t (Gyr)

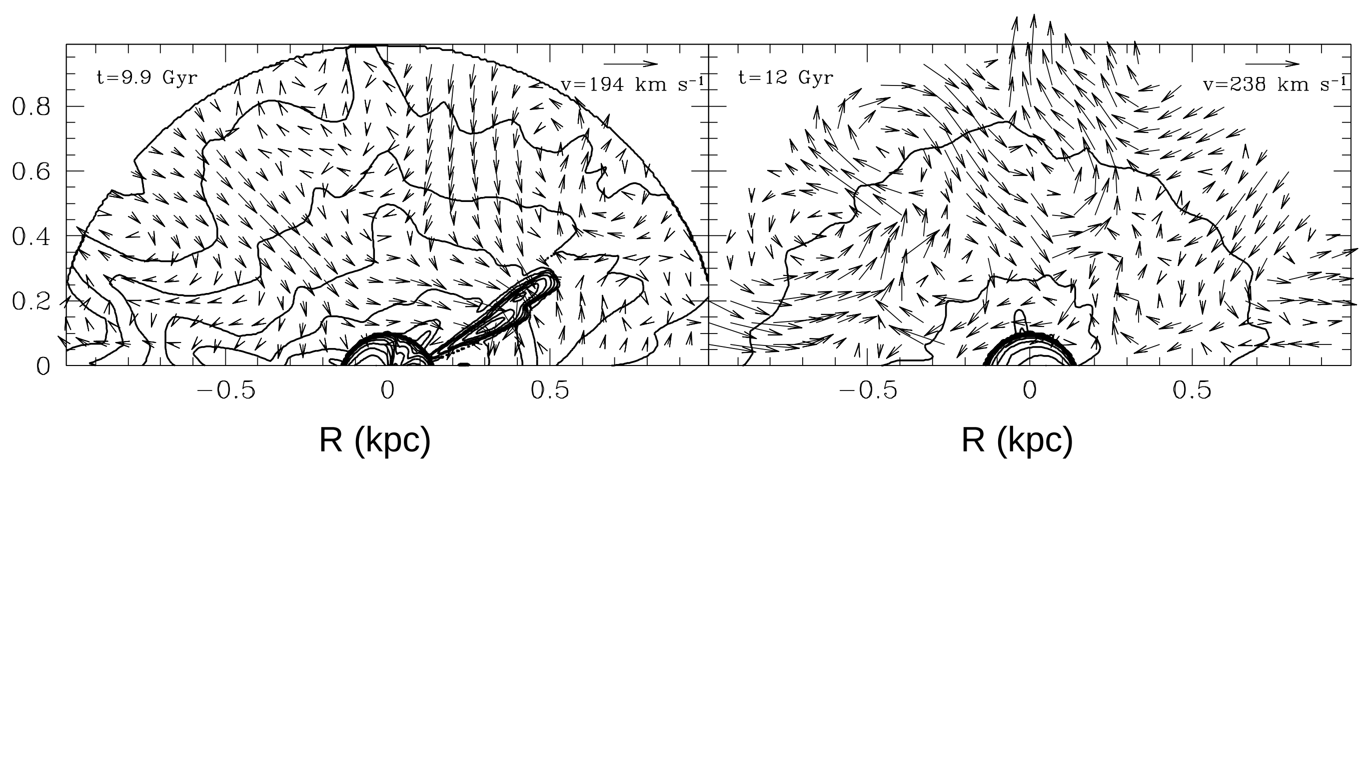

t=9.9 Gyr
v=194 km s^{-1}
0.8
0.6
0.4
0.2
0
−0.5
0
0.5
R (kpc)
t=12 Gyr
v=238 km s^{-1}
−0.5
0
0.5
R (kpc)

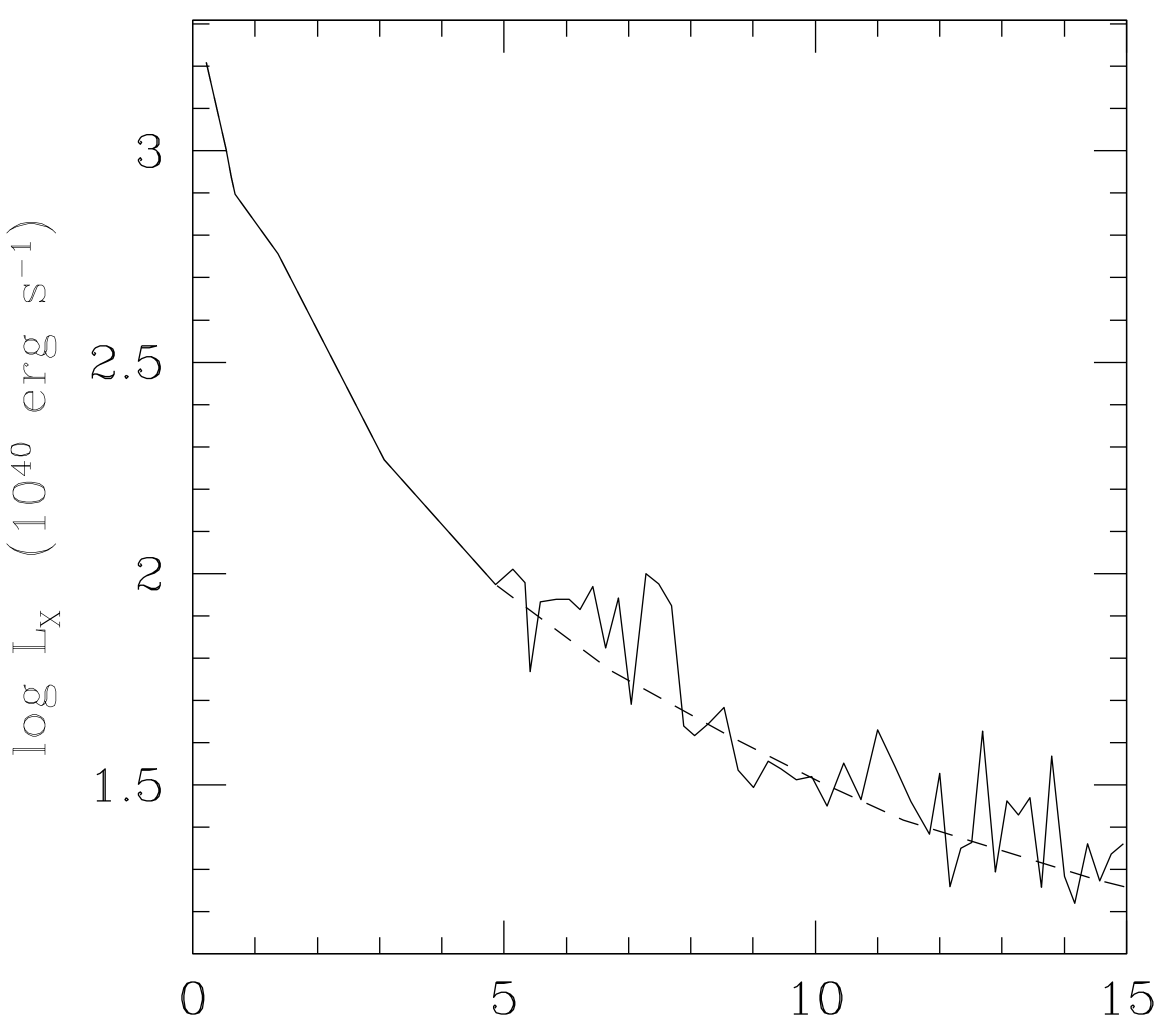

3
2.5
2
1.5
log L_X (10^{40} erg s^{-1})
0
5
10
15
t (Gyr)

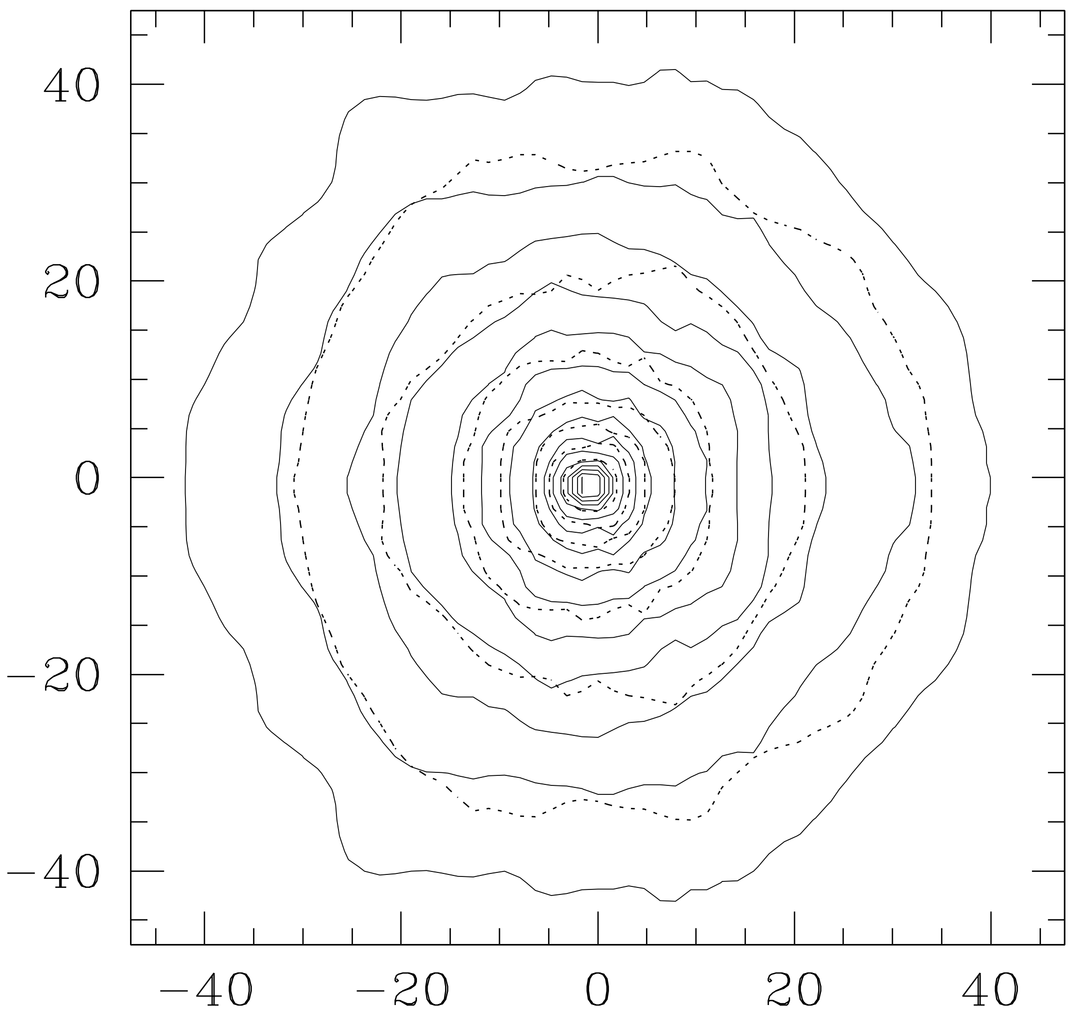

40
20
0
−20
−40
−40
−20
0
20
40

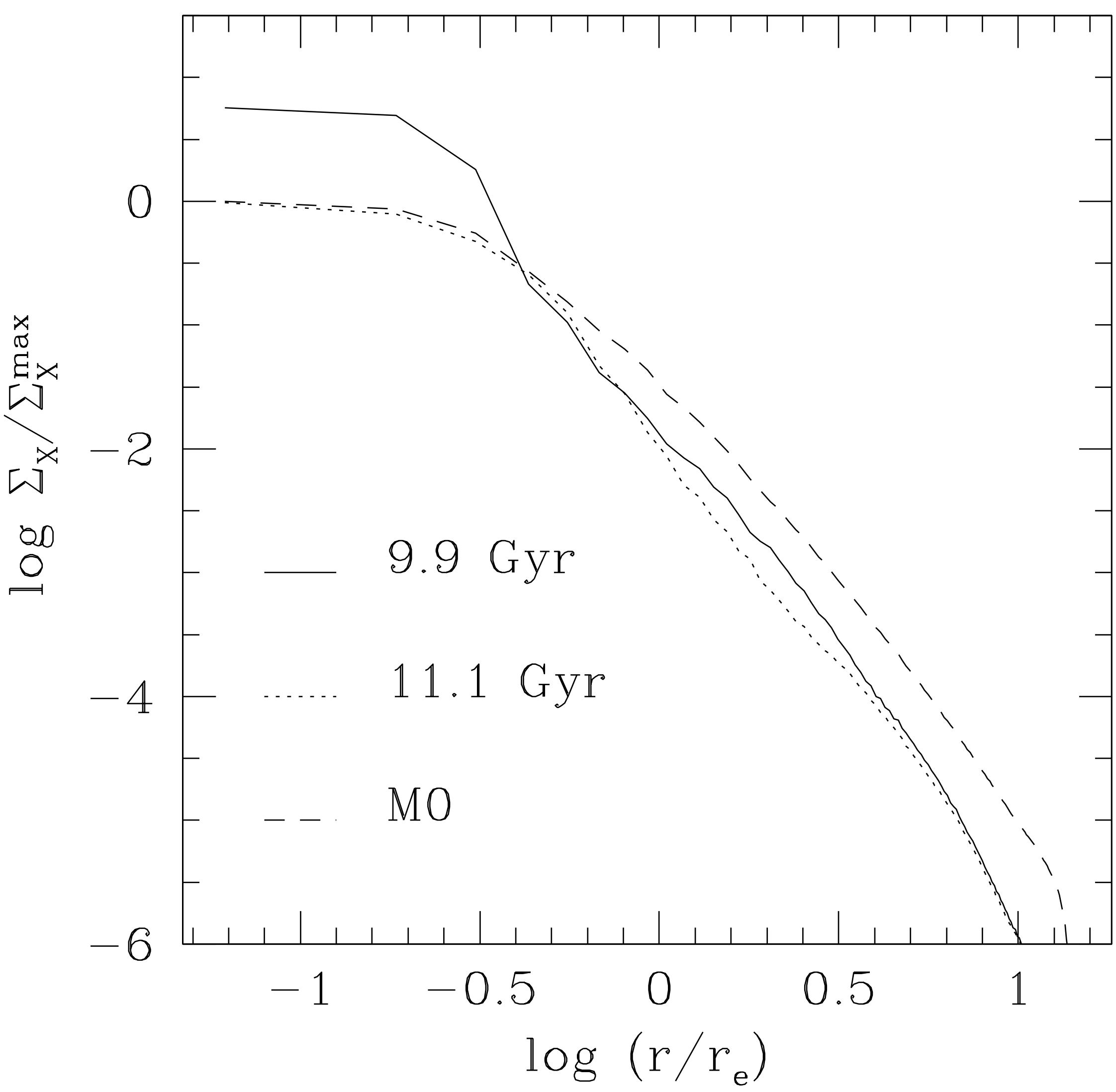

log Σ_X/Σ_X^{max}
0
−2
−4
−6
−1
−0.5
0
0.5
1
log (r/r_e)
9.9 Gyr
11.1 Gyr
MO

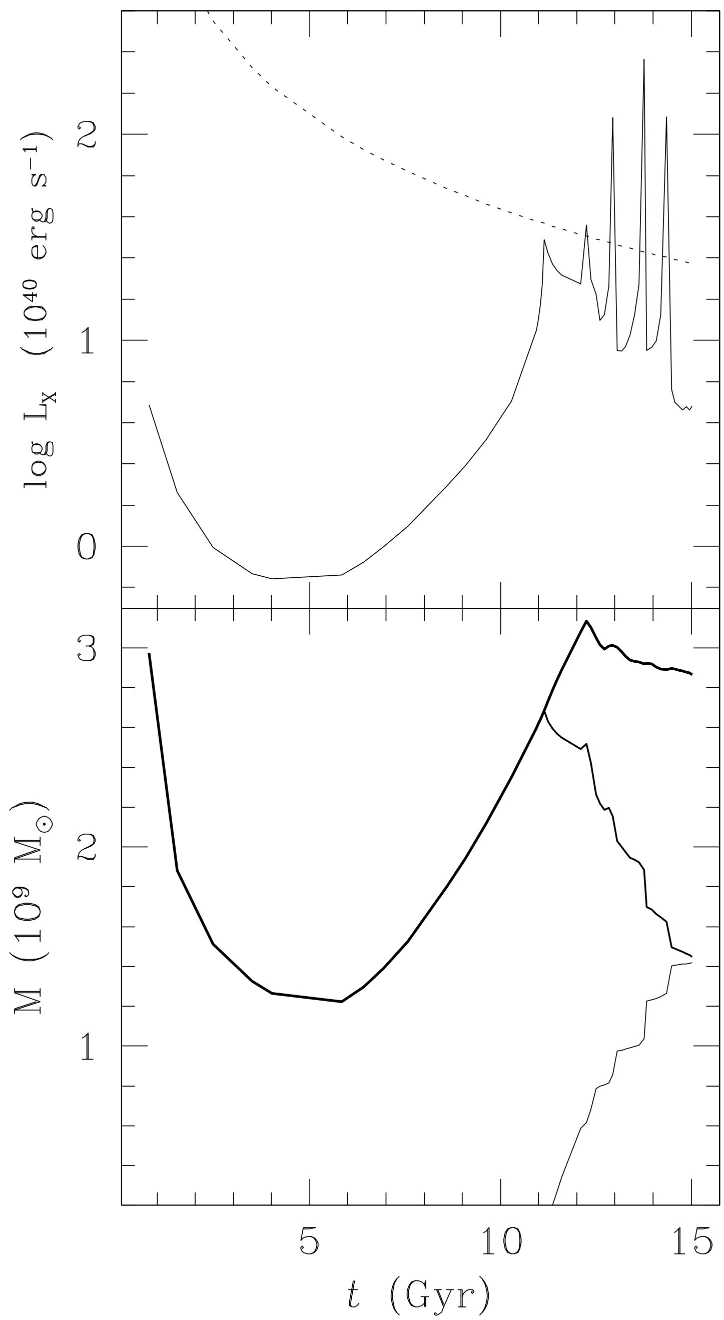

log L_X (10^40 erg s^-1)
0
1
2
M (10^9 M_⊙)
1
2
3
5
10
15
t (Gyr)